

01 Jan 1999

## Preparation of Phase Homogeneous Mn-Zn Ferrite Powder by Spray Pyrolysis

Xinyu Zhao


Baicun Zheng

Hongchen Gu

Chunzhong Li

*et. al.* For a complete list of authors, see [https://scholarsmine.mst.edu/matsci\\_eng\\_facwork/1451](https://scholarsmine.mst.edu/matsci_eng_facwork/1451)

Follow this and additional works at: [https://scholarsmine.mst.edu/matsci\\_eng\\_facwork](https://scholarsmine.mst.edu/matsci_eng_facwork)

 Part of the [Chemistry Commons](#), [Materials Science and Engineering Commons](#), and the [Physics Commons](#)

---

### Recommended Citation

X. Zhao et al., "Preparation of Phase Homogeneous Mn-Zn Ferrite Powder by Spray Pyrolysis," *Journal of Materials Research*, Materials Research Society, Jan 1999.

The definitive version is available at <https://doi.org/10.1557/JMR.1999.0412>

This Article - Journal is brought to you for free and open access by Scholars' Mine. It has been accepted for inclusion in Materials Science and Engineering Faculty Research & Creative Works by an authorized administrator of Scholars' Mine. This work is protected by U. S. Copyright Law. Unauthorized use including reproduction for redistribution requires the permission of the copyright holder. For more information, please contact [scholarsmine@mst.edu](mailto:scholarsmine@mst.edu).

# Preparation of phase homogeneous Mn–Zn ferrite powder by spray pyrolysis

Xinyu Zhao, Baicun Zheng, Hongchen Gu, and Chunzhong Li  
*Institute of Technical Chemical Physics, East China University of Science and Technology,  
Shanghai, People's Republic of China*

Shi Chang Zhang and P. Darrell Ownby<sup>a)</sup>  
*Department of Ceramic Engineering, University of Missouri–Rolla, Rolla, Missouri 65401*

(Received 20 February 1997; accepted 11 March 1999)

Two kinds of aqueous precursor solutions are used to synthesize Mn–Zn ferrite powders: (i) nitrate (NO) precursor—derived from solutions of  $\text{Mn}(\text{NO}_3)_2$ ,  $\text{Zn}(\text{NO}_3)_2$ , and  $\text{Fe}(\text{NO}_3)_3$ ; and (ii) acetate (AC) precursor—derived from solutions of  $\text{Mn}(\text{CH}_3\text{COO})_2$ ,  $\text{Zn}(\text{CH}_3\text{COO})_2$ , and  $\text{Fe}(\text{NO}_3)_3$ . The composition of the powders synthesized from the precursor AC is very uniform, whereas powders derived from the precursor NO have Mn and Zn segregated on the particle surfaces. In addition, the powders synthesized from precursor AC are solid spherical particles with fine porosity, whereas many hollow and fragmented particles are observed in the powder derived from precursor NO. Overall, the properties of Mn–Zn ferrite cores prepared from the precursor AC are superior to those prepared from the precursor NO. The reasons for the differences are explained and described in detail. The AC precursor powders synthesized by spray pyrolysis produced Mn–Zn ferrite cores with good magnetic properties.

## I. INTRODUCTION

In synthesizing multicomponent ceramic powders, it is difficult to obtain phase and composition homogeneous material, especially in complex compositions.<sup>1</sup> It is nearly impossible to achieve this goal by the mechanical milling and blending process. It is also difficult to simultaneously condense several reactants from their vapors in the desired stoichiometry. For some solution methods, such as the chemical coprecipitation and the hydrothermal methods, homogeneity is difficult to achieve because the various constituents precipitate at different pH values.<sup>2–4</sup> These problems can be overcome by the spray pyrolysis (SP) method. The powders synthesized by the SP method are more uniform in composition than those produced by many other techniques because the reaction is confined to micrometer-sized droplets.<sup>5</sup>

Phase segregation may also occur with the spray pyrolysis of multicomponent materials because of the different solubilities of the precursor components, even though it occurs in micrometer scale droplets. One feasible technique to solve this problem is to choose a proper combination of salts so that the different components of the drops precipitate throughout the entire

volume of the drop simultaneously. This study is the first to attempt this approach in detail. The usual spray pyrolysis practice is to use mixed nitrates of each component as precursors, like the NO precursor of the present study. Examples include Mg–Al spinel,<sup>5</sup>  $\text{CoLaO}_3$ ,<sup>6</sup>  $\text{NiFe}_2\text{O}_4$ ,<sup>7</sup>  $\text{ZrO}_2\text{–Y}_2\text{O}_3\text{–Al}_2\text{O}_3$ ,<sup>2</sup>  $\text{Y–Ba–Cu–O}$ ,<sup>8–11</sup>  $\text{Bi–Ca–Sr–Cu–O}$ ,<sup>12</sup> and  $\text{SrTiO}_3$ <sup>13</sup> powders, which were prepared from their mixed nitrates by spray pyrolysis.

Another study using nitrate precursors showed the effect of chelation by adding citric acid and ethylene glycol as chelating agents.<sup>9</sup> There are also some previous studies in which “hybrid” precursors made up of different salt types were used. For instance,  $\text{Al}_2\text{O}_3\text{–Pt}$  composite particles were obtained from a mixture of  $\text{Al}(\text{SO}_4)_3$  and  $\text{H}_2\text{PtCl}_6$ ,<sup>1</sup> and manganese ferrite powders were prepared from a precursor made up of a mixture of a chloride and a nitrate.<sup>14</sup> However, no special attention was paid to how the combination of different salts influenced the composition homogeneity or the particle morphology.

The purposes of this work are as follows: (i) To synthesize phase homogeneous Mn–Zr ferrite powder by SP. Of particular concern is how to choose the proper salt combinations to obtain phase homogeneous solid (non-hollow) particles in the SP process. (ii) To study the properties of the Mn–Zn ferrites prepared from the resulting powders.

<sup>a)</sup>Address all correspondence to this author.

## II. EXPERIMENTAL PROCEDURE

### A. Synthesis of powder

Fig. 1 is the flowchart of the powder synthesis process. Two kinds of aqueous precursors were used to synthesize Mn–Zn ferrite powders: one is a mixture of the dissolved salts  $\text{Fe}(\text{NO}_3)_3 \cdot 9\text{H}_2\text{O}$ ,  $\text{Mn}(\text{NO}_3)_2 \cdot 6\text{H}_2\text{O}$ , and  $\text{Zn}(\text{NO}_3)_2 \cdot 6\text{H}_2\text{O}$ , named precursor NO, and the other is a mixture of the  $\text{Fe}(\text{NO}_3)_3 \cdot 9\text{H}_2\text{O}$ ,  $\text{Zn}(\text{CH}_3\text{COO})_2 \cdot 2\text{H}_2\text{O}$ , and  $\text{Mn}(\text{CH}_3\text{COO})_2 \cdot 4\text{H}_2\text{O}$  aqueous salts, named precursor AC. The nitrate and/or acetate salts were dissolved in deionized water at room temperature in molar ratios and concentrations listed in Table I producing two kinds of precursor solutions. The synthesis apparatus is shown in Fig. 2. The solutions were atomized by a two-fluid atomizer into a quartz tube reactor (inner diameter

38 mm, 1 m long) heated in an electric furnace. The atomically homogeneous aqueous salt solution was atomized into liquid droplets and carried by flowing air into the first heated zone. Evaporation from each droplet proceeded with no increase in temperature until each droplet consisted of precipitated salts with no remaining liquid water. As the temperature then increased, the nitrate salts melted but were retained in their individual spherical particle/droplet entities. They decomposed in the mixed oxide powder spheres as the temperature further increased. The final reactor temperature ranged from 450 to 850 °C. The spray rate of the solutions was 6.0 ml/min, and the pressure of compressed air was 0.45 MPa corresponding to an air flow rate of 125 l/min. The product powders were collected in a filter bag.

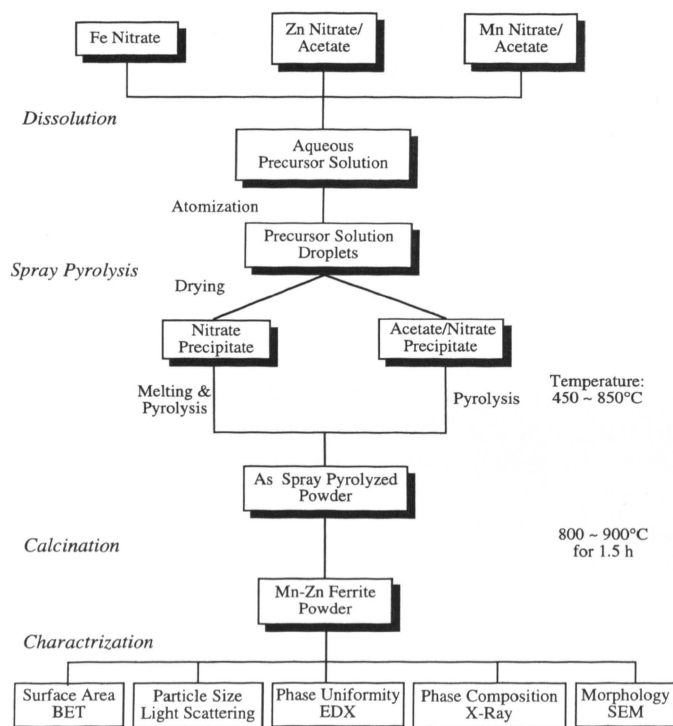


FIG. 1. Powder synthesis flowchart.

### B. Sintering

The Mn–Zn ferrite powders were calcined at 800 to 900 °C for 1.5 h in air and pressed into ring cores at 100 MPa. One percent PVA solution was used as a binder and pressing aid. These samples were sintered at 1320–1350 °C for 3–5 h in air.

### C. Analysis of powders and cores

The morphology of the powders and the surface of the ferrite cores were observed with a scanning electron microscope (SEM) (JSM-35C, JEOL). The particle size and size distribution were determined by a laser light-scattering particle-size analyzer (BI-90, Brookhaven Instruments Co.). The crystalline phases were determined by powder x-ray diffraction (XRD) (DMAX, Rigaku Co.), and the crystallite size was determined by using the XRD line-broadening effect. Fractured cross sections of some of the smaller powder particles were observed by high-resolution electron microscopy (HREM) (JEM-2010, JEOL), and the element distribution was determined by an energy-dispersive x-ray spectrometer (EDX) (ISIS, Link Co.) equipped with HREM. The electric and magnetic properties of the ferrite ring cores ( $\phi 20 \times 10 \times 4$  mm) were measured with a precision

TABLE I. Physical and chemical properties of precursor solutions.

Precursor	Component	Initial concentration $C_0$ (mol/l)	Saturation concentration $C_s$ (mol/L) <sup>a</sup>	Saturation degree, $\alpha$	SS number
NO	$\text{Mn}(\text{NO}_3)_2$	0.255	1.88	0.136	0.37
	$\text{Zn}(\text{NO}_3)_2$	0.210	1.37	0.153	0.42
	$\text{Fe}(\text{NO}_3)_3$	1.035	2.81	0.368	1.0
AC	$\text{Mn}(\text{CH}_3\text{COO})_2$	0.255	1.04	0.245	0.81
	$\text{Zn}(\text{CH}_3\text{COO})_2$	0.210	0.84	0.250	0.83
	$\text{Fe}(\text{NO}_3)_3$	1.035	3.42	0.303	1.0

<sup>a</sup>These  $C_s$  values are for the “hybrid” precursor system which were calculated from  $K_{sp}$ .

inductance-capacitance-resistance (LCR) meter (HP 4284A, Hewlett Packard Co.).

### III. RESULTS

#### A. Morphology

SEM micrographs of Mn–Zn ferrite powders synthesized from the precursor NO and the precursor AC by the SP process at 650 °C are shown in Fig. 3. The particles of the two samples are micrometer- or submicrometer-sized spherical particles. There are some hollow or shell-like particles from the NO precursor, but no hollow or shell-like particles are observed in the AC precursor sample. The mean particle sizes measured by a laser light-scattering particle-size analyzer are 1.35 and 1.63  $\mu\text{m}$  for samples AC and NO, respectively. Since particles from both precursor types had the same initial solution concentration and the same operational conditions, the greater mean particle size of the NO sample

also indicates that there are some hollow particles produced from this precursor. Moreover, it can be seen in Fig. 3(a) that the outer surface of the particle appears smooth, but the internal hollow surface is rough. The particles from both precursors are composed of many nanometer primary particles. The HREM micrographs of the fractured cross sections of smaller particles from each precursor route with their corresponding electron diffraction patterns are shown in Fig. 4. The HREM micrographs [Figs. 4(a), 4(b), and 4(c)] also indicate that hollow particles exist in sample NO, and the particles from both samples are composed of nanometer primary particles. The crystallinity of the sample from NO can be seen to be superior to the sample from AC [Figs. 4(d) and 4(e)].

#### B. Crystalline size

The XRD patterns of powders from precursors AC and NO in Fig. 5 show that the two samples are mixtures of

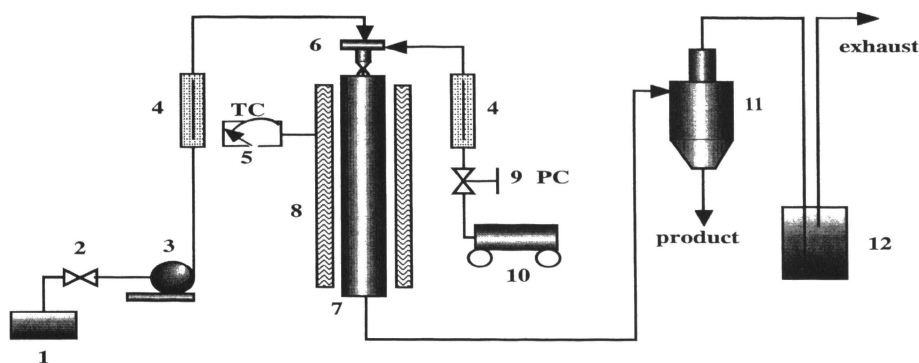


FIG. 2. Experimental apparatus of spray pyrolysis process: (1) precursor solution, (2) control valve, (3) metering pump, (4) flow meter, (5) thermal controller, (6) two-fluid atomizer, (7) quartz reaction tube, (8) resistance furnace, (9) pressure controller, (10) air compressor, (11) bag filter, (12) gas purification column.

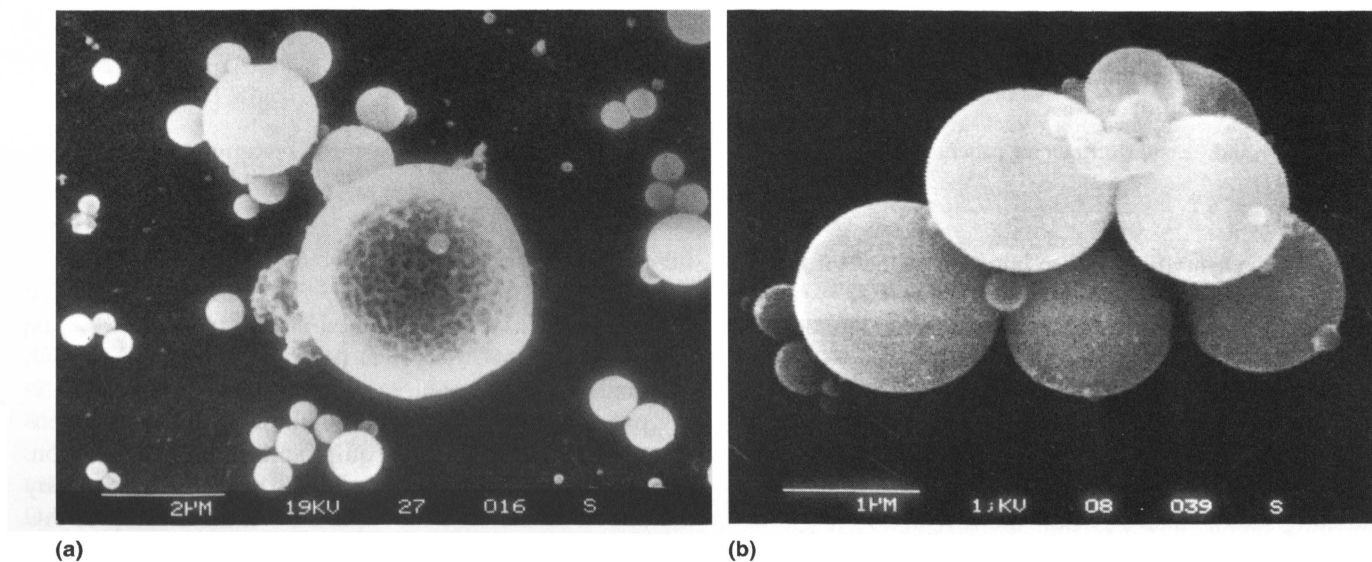


FIG. 3. SEM micrographs of SP synthesized Mn–Zn ferrite powders: (a) precursor NO, (b) precursor AC.

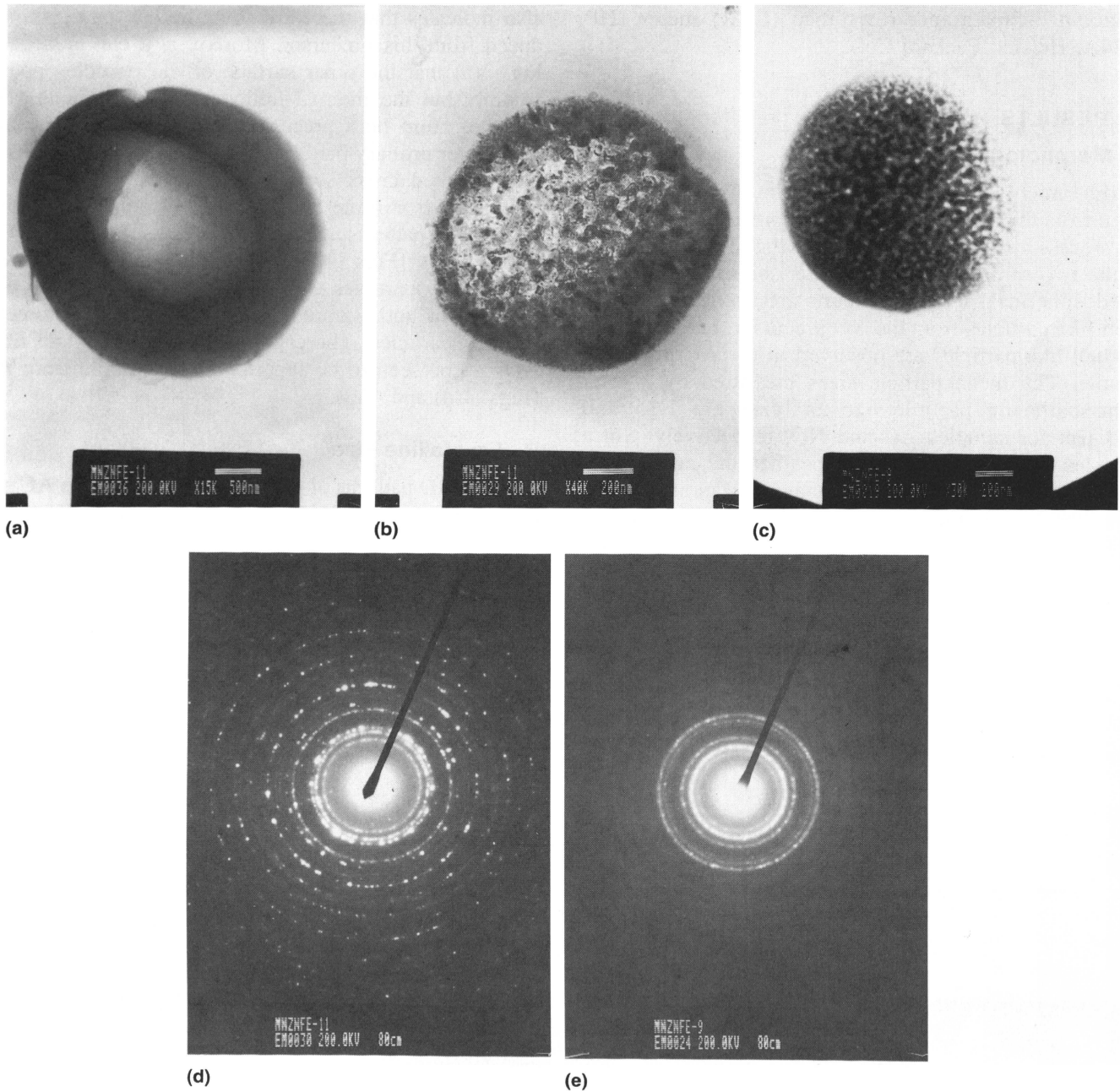


FIG. 4. HREM and electron diffraction patterns of SP synthesized Mn–Zn ferrite powders: (a), (b), and (d), precursor NO; (c) and (e), precursor AC.

the  $\alpha$ - $\text{Fe}_2\text{O}_3$  crystalline phase along with amorphous phase materials. The crystallite size of the  $\alpha$ - $\text{Fe}_2\text{O}_3$  phase was calculated by Scherrer's line-broadening equation.<sup>15</sup>

$$d = \frac{\lambda}{\beta \cos \theta} \quad (1)$$

where  $d$  is the mean crystallite size of  $\alpha$ - $\text{Fe}_2\text{O}_3$ ,  $\lambda$  is the wavelength (1.5405 Å for Cu  $K_\alpha$ ),  $\beta$  is the line-broadening factor, and  $\theta$  is half the diffraction angle of the centroid of the peak (in degrees). The most intense (104) peak ( $2\theta = 33.15^\circ$ ) was used to calculate crystal-

lite size.  $\alpha$ - $\text{Fe}_2\text{O}_3$  powder for calibration was synthesized from 0.5 mol/l  $\text{Fe}(\text{NO}_3)_3 \cdot 9\text{H}_2\text{O}$  solution by the SP process at 650 °C and calcined at 1000 °C for 2 h. The integrated area of the (104) peak for samples AC, NO, and the calibration sample were measured from their x-ray patterns.  $\beta$  was obtained by eliminating the broadening effect caused by the equipment and  $K\alpha_2$  radiation. The crystallite sizes of the  $\alpha$ - $\text{Fe}_2\text{O}_3$  phase determined by the above method are 3.37 and 3.71 nm for samples AC and NO, respectively, which are consistent with the HREM and electron diffraction results.

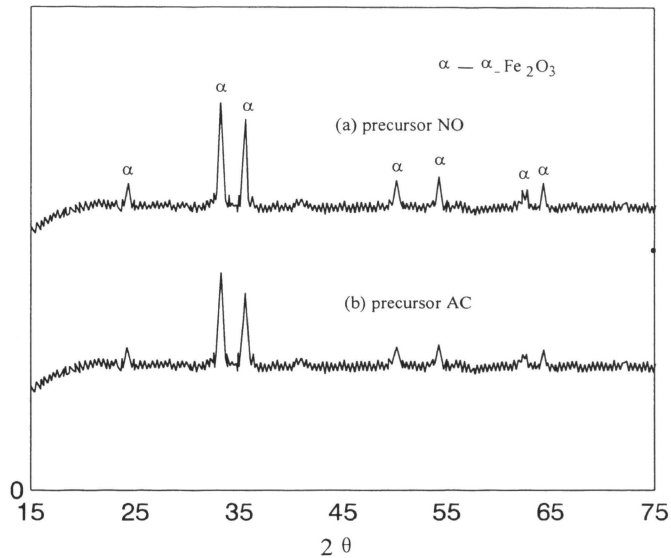


FIG. 5. Comparison of XRD patterns of Mn–Zn ferrite powders synthesized from precursor AC and precursor NO.

### C. Chemical uniformity

The elemental concentration ratios of  $[\text{Mn}]/[\text{Fe}]$  and  $[\text{Zn}]/[\text{Fe}]$  at different locations along cross sections of the solid particles from both precursors were obtained from the quantitative EDX results and plotted against the radial positions ( $r/R$ ) in Fig. 6. As can be seen,  $[\text{Mn}]/[\text{Fe}]$  and  $[\text{Zn}]/[\text{Fe}]$  in sample NO obviously increase with  $r/R$ , indicating that Mn and Zn preferentially segregate to the particle surface. The ratios of  $[\text{Mn}]/[\text{Fe}]$  and  $[\text{Zn}]/[\text{Fe}]$  in sample AC decrease only slightly with  $r/R$  [Fig. 5(b)], and the element distribution is more uniform in the sample AC.

### D. Ferrite phase development

SEM photomicrographs and XRD patterns of Mn–Zn ferrite powder synthesized from the precursor AC at different temperatures are shown in Figs. 7 and 8, respectively. All the powders are micrometer-sized spherical particles, but they were aggregated when they were synthesized at lower reaction temperature ( $<550^\circ\text{C}$ ). The XRD patterns show that the powders prepared below  $550^\circ\text{C}$  are a mixture of oxides and amorphous undecomposed salts. The crystallite oxide content increases with reaction temperature, and Zn ferrite and Mn ferrite phases are formed in the powders synthesized above  $850^\circ\text{C}$ .

Figure 9 shows the XRD patterns of three kinds of calcined Mn–Zn ferrite powders. Powders (a) and (b) were synthesized from the precursors AC and NO, respectively, by the SP process at  $650^\circ\text{C}$ , followed by calcination at  $800^\circ\text{C}$  for 1.5 h. Powder (c) was synthe-

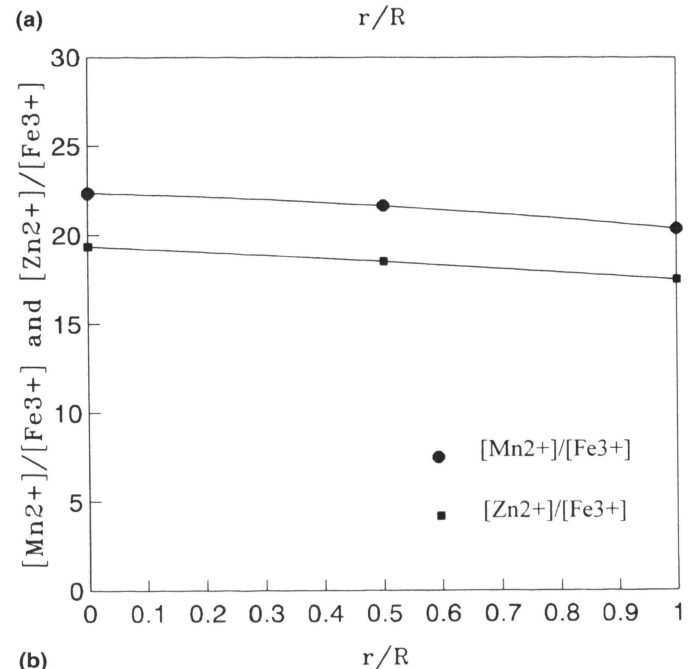
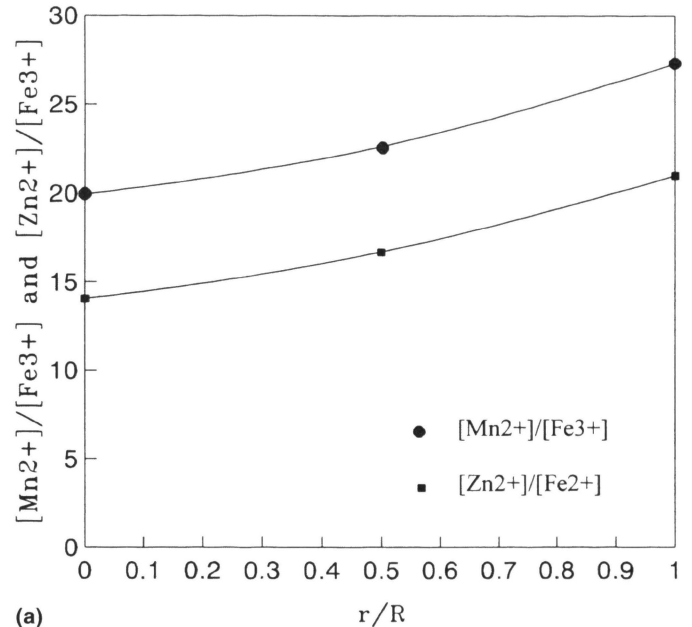


FIG. 6. Element distribution in SP synthesized Mn–Zn ferrite powders: (a) precursor NO, (b) precursor AC.

sized by a conventional solid state reaction method, in which 100–200 nm ZnO,  $\text{Fe}_2\text{O}_3$ , and  $\text{MnCO}_3$  were mixed in a ball mill for 10 h and then calcined under the same conditions as powders (a) and (b). It can be seen from Fig. 9 that all three samples contain  $\alpha\text{-Fe}_2\text{O}_3$  and the Zn ferrite phase, and the relative intensities of the three strongest peaks for the two phases in the three samples are compared in Table II. The relative intensities of the three strongest peaks for each phase are nearly the same in all three samples, which means the effect of powder orientation caused by the preparation of the x-ray

samples can be ignored. The intensities of the (104) peak of the  $\alpha$ -Fe<sub>2</sub>O<sub>3</sub> phase and the (220) peak of the Zn ferrite phase are chosen to determine the fraction converted from iron oxide into zinc ferrite, since the two peaks do not overlap but are near each other. The ratio of the intensity of the two peaks,  $I_F/I_\alpha$ , in the three samples is also tabulated in Table II.

To evaluate the Zn–ferrite phase formation from  $\alpha$ -Fe<sub>2</sub>O<sub>3</sub>, quantitative X-ray analysis was applied. The Zn-ferrite content was determined by

$$\frac{X_F}{X_\alpha} = \left( \frac{I_\alpha}{I_F} \right)_{1:1} \cdot \frac{I_F}{I_\alpha} \quad (2)$$

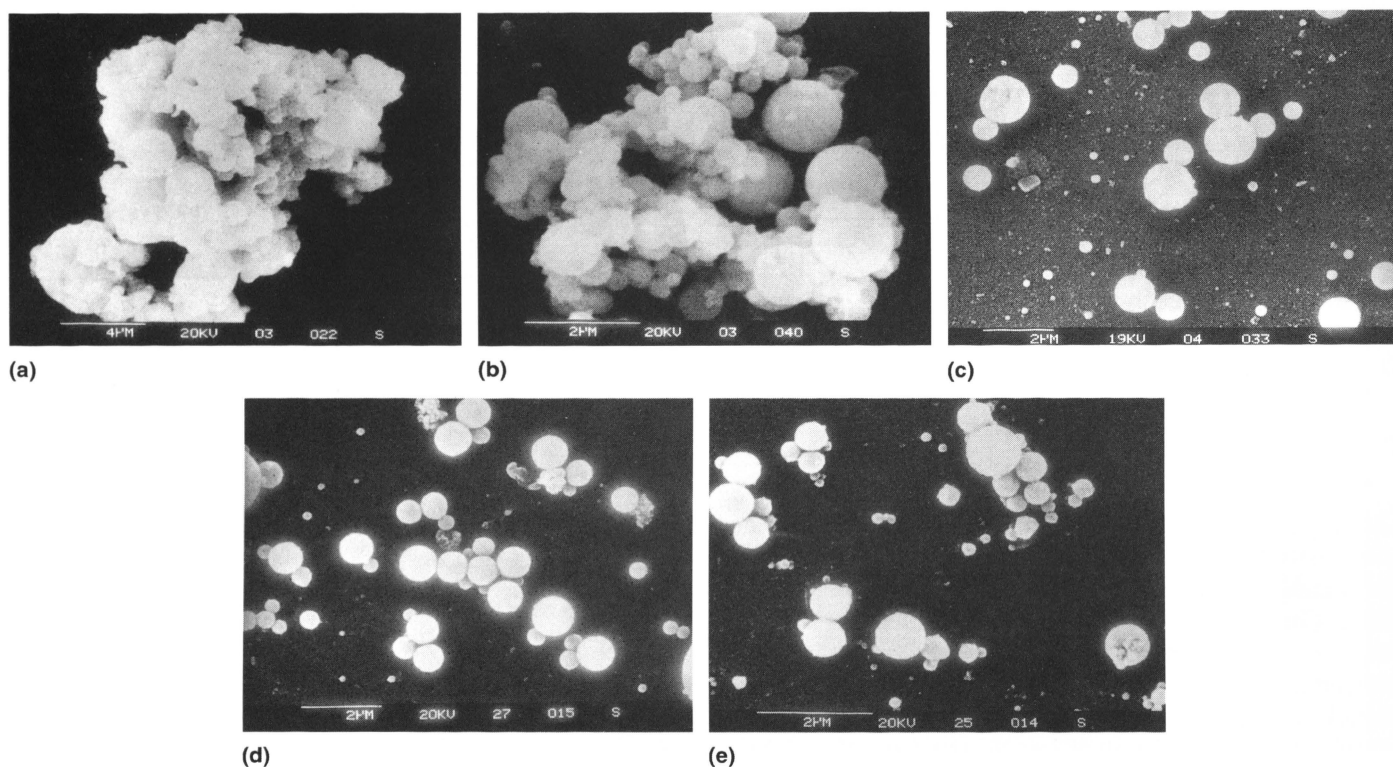


FIG. 7. SEM micrographs of Mn–Zn ferrite powders synthesized at different temperatures (precursor AC): (a) 490 °C, (b) 550 °C, (c) 650 °C, (d) 750 °C, (e) 850 °C.

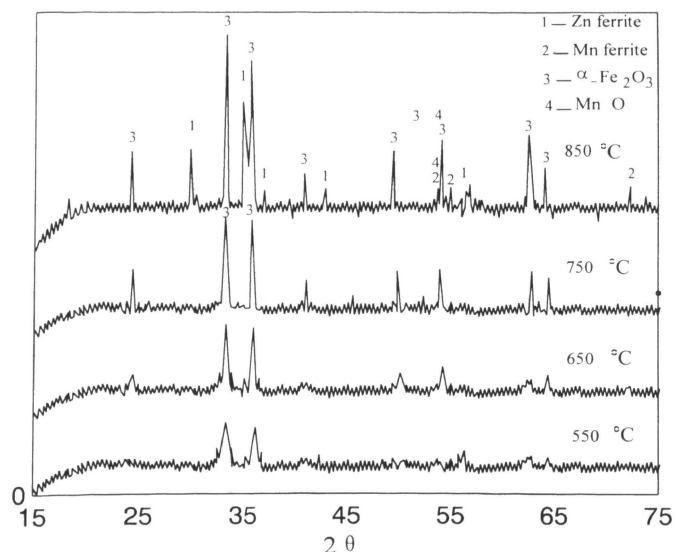


FIG. 8. Mn–Zn ferrite phase development in powders synthesized from precursor AC by SP.

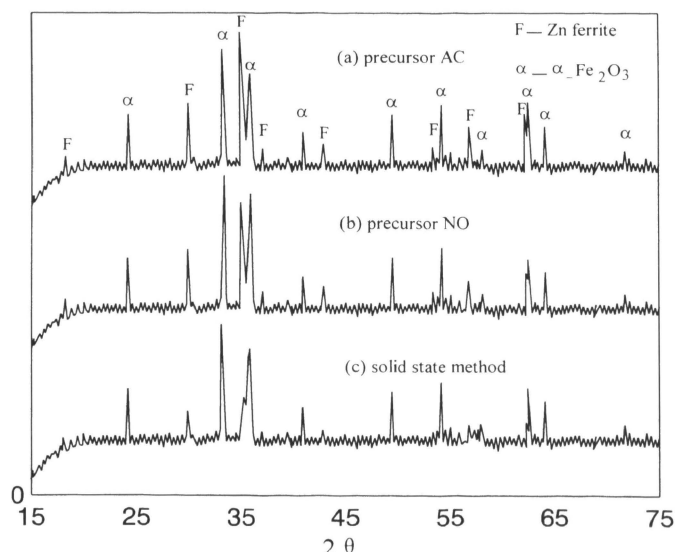


FIG. 9. Comparison of XRD patterns of Mn–Zn ferrite powders synthesized by the SP method and by the solid-state method.

TABLE II. Intensities of XRD peaks and conversion to Zn ferrite in samples (a), (b), and (c) in Fig. 9.

Sample	Intensity (CPS)						Relative intensity (%) <sup>c</sup>						$I_F/I_\alpha$ <sup>d</sup>	$X_F/X_\alpha$
	$\alpha\text{-Fe}_2\text{O}_3$ <sup>a</sup>			Zn ferrite <sup>b</sup>			$\alpha\text{-Fe}_2\text{O}_3$			Zn ferrite				
	$I_{\alpha 1}$	$I_{\alpha 2}$	$I_{\alpha 3}$	$I_{F1}$	$I_{F2}$	$I_{F3}$	$I_{\alpha 1}$	$I_{\alpha 2}$	$I_{\alpha 3}$	$I_{F1}$	$I_{F2}$	$I_{F3}$		
(a)	4323	3751	2581	4489	2413	2256	100	86.8	59.7	100	53.8	50.3	0.558	0.715
(b)	4331	3836	2601	3705	2070	1991	100	88.6	60.1	100	55.9	53.7	0.478	0.613
(c)	4700	4064	2652	2346	1329	1271	100	86.5	56.4	100	56.7	54.2	0.283	0.370

<sup>a</sup>The d value and Miller indices of  $I_{\alpha 1}$ ,  $I_{\alpha 2}$ , and  $I_{\alpha 3}$  are 2.70(104), 2.52(110), 1.70(116), respectively.

<sup>b</sup>The d value and Miller indices of  $I_{F1}$ ,  $I_{F2}$ , and  $I_{F3}$  are 2.54(311), 2.98(220), 1.48(440), respectively.

<sup>c</sup>The relative intensities of  $\alpha\text{-Fe}_2\text{O}_3$  phase regard its strongest peak intensity  $I_{\alpha 1}$  as 100% and that of Zn ferrite regard  $I_{F1}$  as 100%.

<sup>d</sup> $I_F$  is the intensity of (220), i.e.,  $I_{F2}$ , and  $I_\alpha$  is the intensity of (104), i.e.,  $I_{\alpha 1}$ .

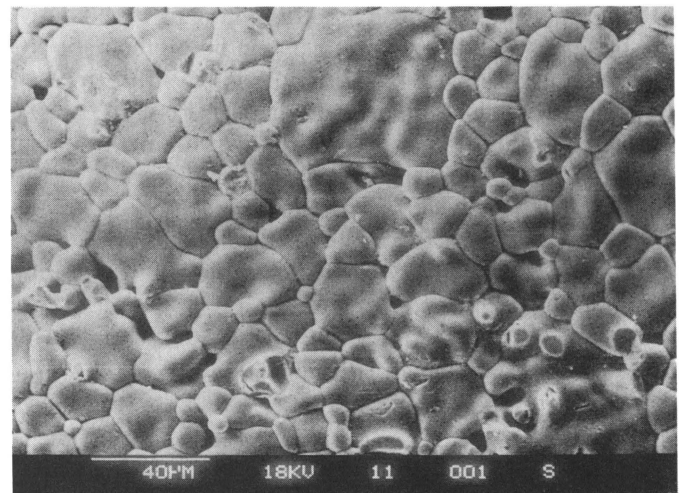
TABLE III. Comparison of properties of Mn–Zn ferrite cores prepared from different precursors.

Sample	Initial permeability $\mu_i$	Saturation magnetic flux density $B_S$ (mT)	Curie temperature $\theta_f$ (°C)	Power loss $\tan \delta/\mu_i$ ( $\times 10^{-6}$ )
Sample NO	4200–4700	405	$\geq 140$	$\geq 6.5$
Sample AC	5000–5500	405	$\geq 140$	$\leq 4.5$

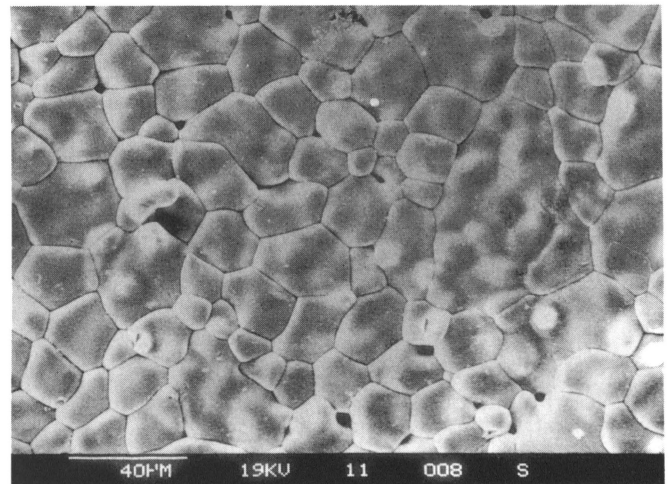
The calibration factor  $(I_F/I_\alpha)_{1:1}$  is defined as the intensity ratio of the Zn–ferrite to  $\alpha\text{-Fe}_2\text{O}_3$  peaks on x-ray patterns taken from equal weight mixtures of both phases. The experimental result indicates that the  $(I_F/I_\alpha)_{1:1}$  ratio is 0.78. The  $X_F/X_\alpha$  ratios in the three samples (a), (b), and (c) are calculated to be 0.715, 0.613, and 0.370, respectively, and are also listed in Table II. It can be seen that the conversion to Zn ferrite in powder (a) is higher than in powder (b) and is lowest in powder (c). Therefore, the SP synthesized Mn–Zn ferrite powders are superior in this regard to the material derived from the conventional solid state method, and the powder synthesized from precursor AC is better than that synthesized from precursor powder NO.

### E. Magnetic properties of the sintered ferrites

The properties of Mn–Zn ferrite cores prepared from Mn–Zn ferrite powders synthesized by the SP process at 850 °C are shown in Table III. Saturation magnetic flux density,  $B_s$ , and the Curie temperature,  $\theta_f$ , of the two samples are the same. The initial permeability,  $\mu_i$ , of sample AC is higher than that of sample NO, and power loss  $\tan \delta/\mu_i$  of sample AC is lower than that of sample NO. Therefore, the magnetic properties of sample AC are better than those of sample NO. Figure 10 shows the SEM photomicrographs of the surface of the two sintered samples from the two types of precursors. The average grain size in samples AC and NO are 14.7 and 12.3  $\mu\text{m}$ , respectively.



(a)



(b)

FIG. 10. SEM micrographs of the surface of Mn–Zn ferrite ring cores prepared from SP synthesized powders: (a) precursor NO, (b) precursor AC.

## IV. DISCUSSION

### A. Particle morphology

For a multicomponent system, the particle morphology depends mainly on the precipitation behavior of the first-



precipitated component (FPC). Precipitation of the FPC uniformly within the entire volume of the droplet favors solid particle formation, while surface precipitation of the FPC results in hollow particles. The FPC can be determined by comparing the initial saturation degree  $\alpha$  of each component, that is, the ratio of the initial concentration  $C_o$  to the equilibrium maximum solubility concentration  $C_s$ . Strictly speaking, the degree of supersaturation should be used, but so far the supersaturation cannot be determined for SP conditions. Nevertheless, the degree of saturation  $\alpha$  can be used to compare the relative resistance to precipitation of the salts.<sup>16</sup> The smaller the  $\alpha$  is, the more resistant to precipitation is the salt. From Table I we can see that the  $\alpha$  of  $\text{Fe}(\text{NO}_3)_3$  is the largest of the three components in both precursor NO and precursor AC. In addition, the solubility of  $\text{Fe}(\text{CH}_3\text{COO})_3$  is higher than that of  $\text{Fe}(\text{NO}_3)_3$ ,<sup>17</sup> so  $\text{Fe}(\text{NO}_3)_3$  is the FPC in both of the two multicomponent precursors.

It has been indicated by previous research on single-component systems that a large difference between the critical supersaturation  $C_{ss}$  and the equilibrium saturation  $C_s$  of the precursor favors volume precipitation.<sup>18</sup> The difference ( $C_{ss} - C_s$ ) for  $\text{Fe}(\text{NO}_3)_3$  in a multicomponent system can be calculated from the solubility product  $K_{sp}$

$$C_{ss} - C_s = \frac{(S^* - 1)k_{sp}}{[\text{NO}_3^-]^3} \quad (3)$$

where  $S^*$  is the critical supersaturation for  $\text{Fe}(\text{NO}_3)_3$ , and  $[\text{NO}_3^-]$  is the concentration of the  $\text{NO}_3^-$  ion in the precursor solution. It can be seen from equation (3) that the difference ( $C_{ss} - C_s$ ) is inversely proportional to the third power of  $[\text{NO}_3^-]$ ; therefore ( $C_{ss} - C_s$ ) greatly decreases with  $[\text{NO}_3^-]$ . For precursor NO, addition of  $\text{Mn}(\text{NO}_3)_2$  and  $\text{Zn}(\text{NO}_3)_2$  to the  $\text{Fe}(\text{NO}_3)_3$  increases the  $\text{NO}_3^-$  concentration in the solution and results in a decrease of ( $C_{ss} - C_s$ ) of  $\text{Fe}(\text{NO}_3)_3$ . On the other hand, for precursor AC, addition of  $\text{Mn}(\text{CH}_3\text{COO})_2$  and  $\text{Zn}(\text{CH}_3\text{COO})_2$  to the  $\text{Fe}(\text{NO}_3)_3$  does not affect the value of the ( $C_{ss} - C_s$ ) of the  $\text{Fe}(\text{NO}_3)_3$ . As a result, the difference ( $C_{ss} - C_s$ ) of  $\text{Fe}(\text{NO}_3)_3$  in precursor AC is greater than that in precursor NO. Precursor AC favors volume precipitation of  $\text{Fe}(\text{NO}_3)_3$  and consequently it results in solid porous particle formation compared with hollow shell-like porous particles formed from precursor NO.

The melting temperatures of the nitrates are very low. They are 47.2 °C, 36.4 °C, and 25.8 °C for  $\text{Fe}(\text{NO}_3)_3 \cdot 9\text{H}_2\text{O}$ ,  $\text{Mn}(\text{NO}_3)_2 \cdot 6\text{H}_2\text{O}$ , and  $\text{Zn}(\text{NO}_3)_2 \cdot 6\text{H}_2\text{O}$ , respectively. During the thermal decomposition process the crystalline water leaves first, in steps. Above 100 °C, the decomposition gas permeability through the molten salts is reduced, resulting in an increased internal gas pressure that leads to hollow or fragmented particles.<sup>19</sup> Melting temperatures of the acetates

are relatively high. For example,  $\text{Zn}(\text{CH}_3\text{COO})_2 \cdot 2\text{H}_2\text{O}$  melts at 237 °C. The acetates improve the gas permeability through the particles by acting as a network frame for the molten nitrate, allowing easier release of the gas from decomposition, preventing pressure buildup and consequent deformation of the particles. This explains why precursor AC is superior to precursor NO for synthesis of porous solid Mn–Zn ferrite particles.

Generally, the value of ( $C_{ss} - C_s$ ) in hybrid salt precursors with different anions is greater than that in salt precursors with the same anion, so hybrid precursors with a proper combination of different kinds of salts favors solid particle formation in multicomponent systems.

## B. Phase segregation

Phase distribution in multicomponent particles depends greatly on the precipitation sequence of the components. If the degrees of saturation of the different components are nearly the same, simultaneous precipitation of the different components will occur. When precipitation in the total droplet volume is satisfied for each component, solid particles with uniform phase distribution will be obtained. On the other hand, if the difference between  $\alpha$  values of the components is large, the components with a higher  $\alpha$  will precipitate first, producing the so-called sequential precipitation,<sup>1</sup> which may result in phase segregation.

The saturation degree  $\alpha$  for each component in the hybrid salt precursors with different anions is the same.

$$\alpha = C_o/C_s \quad (4)$$

A dimensionless number, SS, is defined as the ratio of the  $\alpha$  of the later-precipitated component (LPC) to the  $\alpha$  of the FPC and is used to measure the tendency for simultaneous precipitation<sup>20</sup>

$$\text{SS} = \alpha_{\text{LPC}}/\alpha_{\text{FPC}} \quad (5)$$

SS numbers range from 0 to 1. Greater SS numbers (especially SS ~1) favor simultaneous precipitation, and smaller SS numbers result in sequential precipitation. For the precursors used in this study, the FPC is  $\text{Fe}(\text{NO}_3)_3$ , the LPC are salts of Mn and Zn. The  $\alpha$  and the SS of each component in the two precursors are shown in Table I. The SS numbers of  $\text{Mn}(\text{CH}_3\text{COO})_2$  and  $\text{Zn}(\text{CH}_3\text{COO})_2$  in precursor AC are 0.81 and 0.83, respectively, both close to 1.0. Those of  $\text{Mn}(\text{NO}_3)_2$  and  $\text{Zn}(\text{NO}_3)_2$  in precursor NO are 0.37 and 0.42. It can be concluded that precursor AC favors simultaneous precipitation, and it also favors volume precipitation, so solid particles with uniform phase distribution are obtained [Fig. 3(b)]. Phase segregation in the particles derived from precursor NO is due to sequential precipitation according to the lower SS numbers.

Combining Eq. (4) with Eq. (5), the SS numbers can be transformed as

$$SS = \frac{C_{oLPC}/C_{oFPC}}{C_{sLPC}/C_{sFPC}} \quad (6a)$$

$$SS = \frac{C_{oLPC}/C_{sLPC}}{C_{oFPC}/C_{sFPC}} \quad (6b)$$

From Eq. (6a), it can be seen that for a given initial molar ratio,  $C_{oLPC}/C_{oFPC}$ , in the composite powder we should choose a combination of precursor salts so that the ratio,  $C_{sLPC}/C_{sFPC}$  of the equilibrium concentration is nearly equal to the initial molar ratio  $C_{oLPC}/C_{oFPC}$ , which will satisfy  $SS \sim 1$  and favor uniform phase distribution.

From Eq. (6b), the concentration limitation in the composite for a given combination of precursor salts can be determined.

### C. Formation of ferrite phase

The formation of zinc ferrite by a solid state reaction is a typical diffusion-controlled process,<sup>21</sup> and the reaction rate can be described by the Jander equation<sup>22</sup>

$$(1 - (1 - \varphi)^{1/3})^2 = \left(\frac{2K}{r_o^2}\right)t \quad (7)$$

where  $\varphi$  is the fraction reacted,  $r_o$  is the initial particle radius,  $K$  is the reaction rate constant, and  $t$  is the reaction time. From Eq. (7), it can be seen that the smaller  $r_o$  results in a more rapid reaction rate.  $r_o$  can be regarded as the diffusion distance of ions and obviously, the reaction rate increases with a decrease in the diffusion distance. The particle size of the ZnO, Fe<sub>2</sub>O<sub>3</sub>, and MnCO<sub>2</sub> in the raw material powder (c) is 100–200 nm, while the particle sizes of the SP synthesized powders (a) and (b) are 1.35 and 1.62  $\mu\text{m}$ , respectively. It first appears that  $r_o$  for powder (c) is less than that of powders (a) and (b). However, the SP synthesized particles are comprised of nanometer primary particles. The HREM photomicrographs indicate that the size of the primary particles is 20 nm in powders (a) and (b), which is much less than the particle size of powder (c).

Ito *et al.*<sup>23</sup> studied the effects of grinding ZnO and Fe<sub>2</sub>O<sub>3</sub> on the rate of formation of Zn ferrite, and found that better mixing of ZnO and Fe<sub>2</sub>O<sub>3</sub> will increase the contact area between them and enhance the rate of ferrite formation. The SP synthesized Mn–Zn ferrite powders are composed of very uniformly distributed nanometer primary particles. Such uniformity cannot be achieved by mechanical mixing. The special microstructure of SP synthesized Mn–Zn ferrite powder decreases the diffusion distance for the ions and increases the contact area between reactants, leading to a higher conversion to the

Zn ferrite in powders (a) and (b) than that in powder (c). In the same way, the segregation of elements Mn and Zn at the particle surface in powder (b) influences the mixing of reactants, and results in the relatively low conversion to ferrite in powder (b) compared with that in powder (a). In addition, segregation in the SP powders was limited to the size of a single micrometer-sized particle, which may be much smaller than the aggregates existing in powder (c).

Toolenaar and Verhees<sup>24</sup> found that reactive sintering of ferrite is accompanied by a microscopic expansion and an increase of the average pore size, which will severely influence the densification and the properties of the final products. They demonstrated that the best way to minimize the increase in pore size during reaction is to use homogeneously mixed smaller particles. From this point of view, the powder synthesized from precursor AC by the SP process is the best method to achieve this goal. The above analyses are aimed at the formation of Zn ferrite, but they are also valid for formation of Mn ferrite because of the similarity of formation of the ferrites. Mn–Zn ferrite cores with good properties can be made from SP synthesized powders, and magnetic properties can be further improved if the composition of the precursor solution and the sintering process are optimized.

### V. CONCLUSIONS

For multicomponent powders produced by the SP process, hybrid salt precursors with different anions maintain a higher value of  $(C_{ss} - C_s)$  and favor volume precipitation and solid particle formation. Multicomponent precursors with the greatest SS numbers result in the simultaneous precipitation of the component salts and a uniform phase distribution. Precursors with smaller SS numbers result in a sequential precipitation and phase segregation. Solid Mn–Zn ferrite powders with uniform phase distribution was synthesized by the SP process from the hybrid precursor salts of Fe(NO<sub>3</sub>)<sub>3</sub>, Mn(CH<sub>3</sub>COO)<sub>2</sub>, and Zn(CH<sub>3</sub>COO)<sub>2</sub>. The SP synthesized powders are favorable for ferrite formation because of a very uniform distribution of nanometer primary oxide particles. Mn–Zn ferrite cores with good magnetic properties were prepared from these powders.

### ACKNOWLEDGMENTS

We gratefully acknowledge the support for this research by the University of Missouri Research Board, the Chinese National Natural Science Fund, and the Chinese National Engineering Research Center of Ultra-fine Powders.

## REFERENCES

1. G.L. Messing, S.C. Zhang, and G.V. Jayanthi, *J. Am. Ceram. Soc.* **76**(11), 2707 (1993).
2. D. Vollath and K.E. Sickafus, *J. Mater. Sci.* **28**, 5943 (1993).
3. M. Rozman and M. Drogenik, *J. Am. Ceram. Soc.* **78**(9), 2449 (1995).
4. A. Grurav, T.T. Kodas, P. Pluym, *et al.*, *Aerosol Sci. Technol.* **19**(4), 411 (1993).
5. Y. Suyama and A. Kato, *Ceram. Int.* **8**(1), 17 (1982).
6. H. Imai, K. Takami, and M. Naito, *Mater. Res. Bull.* **19**(10), 1293 (1984).
7. A.M. Gadalla and H-F. Yu, *J. Mater. Res.* **5**, 2923 (1990).
8. T.T. Kodas, E.M. Engler, V.Y. Lee, *et al.*, *Appl. Phys. Lett.* **52**(19), 1622 (1988).
9. C.H. Chao and P.D. Ownby, *J. Mater. Sci.* **30**, 6136 (1995).
10. S. Chadda, T.L. Ward, A. Carin, T.T. Kodas, *et al.*, *J. Aerosol Sci.* **22**(5), 601 (1991).
11. W. Lo, O.A. Cardwell, S.L. Dung, and R.G. Barter, *J. Mater. Res.* **11**, 39 (1996).
12. N. Tohge, M. Tatsumisago, and T. Minami, *J. Am. Ceram. Soc.* **74**(9), 2117 (1991).
13. Y. Senzaki, J. Caruso, M.J. Hampden-Smith, T.T. Kodas, *et al.*, *J. Am. Ceram. Soc.* **78**(11), 2973 (1995).
14. Q. Li and C.M. Sorensen, *Aerosol Sci. Tech.* **19**(4) (1993).
15. *X-Ray Diffraction Procedure for Polycrystalline and Amorphous Materials*, 2nd. edited by H.P. Klug and L.E. Alexander (John Wiley & Sons, New York, 1974), p. 534.
16. S.C. Zhang and G.L. Messing, *J. Am. Ceram. Soc.* **73**(1), 61 (1990).
17. *CRC Handbook of Chemistry and Physics*, 70th edition, edited by R.C. Weast, (CRC Press, Florida, 1989).
18. G.V. Jayanthi, S.C. Zhang, and G.L. Messing, *Aerosol Sci. Technol.* **19**(4), 478 (1993).
19. D.W. Sproson and G.L. Messing, *Ceram. Powder Sci.*, edited by G.L. Messing *et al.* (Am. Ceram. Soc., Columbus, OH, 1989), p. 99.
20. Xinyu Zhao, MS Thesis, East China University of Science and Technology, Shanghai.
21. J.F. Duncan and D.J. Steward, *Trans. Farad. Soc.* **63**, 1031 (1967).
22. F.J.C.M. Toolenaar, *J. Mater. Sci.* **24**, 1089 (1989).
23. M. Ito, M. Senna, and H. Kuno, in *Ferrites*, (Proceedings of International Conference on Ferrites, **ICF-4**, Tokyo, Japan, 1980), p. 50.
24. F.J.C.M. Toolenaar and M.T.J. Verhees, *J. Mater. Sci.* **23**, 856 (1988).